# Experimental and computational investigation of cyclic mechanical behavior of sintered iron

Markus Schneider [a,b], Huang Yuan [a,*]

[a] University of Wuppertal, Department of Mechanical Engineering, Wuppertal, Germany
[b] GKN Sinter Metals Engineering GmbH, Radevormwald, Germany

ABSTRACT

Sintered metals have found wide applications in mechanical design for their low manufacturing costs. The present paper deals with a sintered iron powder material (ASC 100.29) which is specially manufactured for experimental and computational investigations. The material has been tested under both monotonic and cyclic loading conditions. Fully reversed fatigue tests have been performed with different material porosities, strain loading ratios and loading amplitudes. Cyclic stress–strain curves and corresponding fatigue life curves are identified. Experiments confirm that the cyclic loading reduces material fracture strain dramatically and the mean strain does not influence fatigue life, regardless of material porosities. The resulting hysteresis loops have been investigated concerning the hardening mechanism. The computational simulations show that the superposition of a nonlinear kinematic and isotropic hardening model can describe experiments reasonably. Computational verification reveals that the identified material model will hardly predict ratcheting behavior of the material.

© 2011 Elsevier B.V. All rights reserved.

## 1. Introduction

Sintered powder metals (PM) offer the freedom of material design, almost full material utilization, low fabrication costs, few production steps and a controlled density. A controlled density is essential for filter-elements and self-lubricated bearings. These advantages are responsible for increasing applications in the automotive industry.

In the PM-industry it is common to present engineering fatigue data by means of $S$–$N$ curves. The $S$–$N$ relationship is determined by stress-controlled tests. The resulting material response, in the form of strains or bending deflections, will not be measured. A commonly used specimen is the rectangular bending bar specimen [6]. The reasons for that experimental setup are the high testing frequency ($f \approx 75$ Hz) and simplicity. For most industrial applications the PM components will mainly be tested under the stress-controlled condition for the high cycle fatigue (HCF) property. A good overview about the HCF tests for sintered specimens prepared from a pure iron powder (ASC 100.29) can be found in [11]. Weiss and Danninger compiled several $S$–$N$ curves for different chemical compositions, sintering temperatures and densities [25]. Beiss and Dalgic [4] investigated the influence of the pore morphology on the fatigue strength. It is pointed out that the main effects to HCF strength are the density and the sintering temperature. A secondary effect is also noticeable from pore shape irregularities. The material

behavior is dominated by the largest pores (10%) [4]. Rutz and Murphy focused on the mean pore spacing and draw similar conclusions [22]. Using the suggestions of Murakami and Gumbel's statistics of extremes, Beiss and Lindlohr suggested that it is more important to improve the hardness than to eliminate extremely large pores [5]. Beiss proposed a power law to relate fatigue properties with specimen's density. Moreover the Larson-Miller parameter was proposed to contract the sintering time and temperature [3]. Brandt and Sonsino investigated the effect of different mean stresses on the endurance strength of Fe-Mo-Ni alloys. Four stress loading ratios $R_\sigma = 0, -1, -2, -3$ are realized. It is known that mean stress affects fatigue life significantly [7].

With increasing the application spectrum, the finite life design is now interesting for the PM materials. In this sense low cycle fatigue becomes a research topic for PM. For strain-controlled lifetime predictions of PM-components the situation is less advanced. Recent methods of strength assessment are based on local concepts. At high loadings ($N_f \leqslant 10^4$) the strains become dominant in life prediction [13]. Many sintered components, e. g. gears, conrods and oil-pumps, are applied under a dynamic regime of high loading. Stress peaks during the operation caused by transient overload conditions lead to localized plastic strains at notched geometries [13]. This effect can be described by cyclic strain-controlled fatigue (LCF). To predict a finite life, a reliable constitutive equation for the cyclic plasticity is substantial. Machmeier [19] presented several cyclic stress–strain curves and corresponding fatigue strain life curves for sinter forged alloys. The effect of inclusions on the crack propagation is investigated. Fatigue life data

---

presented as Manson-Coffin plots have been reported on phosphorus alloy steel, Ni–Mo alloys and some austenitic steels [14]. Lados and Apelian [18] compiled cyclic stress–strain curves for sintered iron and an Fe–Ni–Mo alloy. It is mentioned that pure iron shows a cyclically softening behavior at all strain levels ($\epsilon_{a\,max} \approx 0.35\%$). Some stress-controlled hysteresis loops are presented which do not correspond to the cyclic stress–strain curves. Kraft and Riedel [16] presented a LCF-damage model based on Heitmann's parameter which is based on elastic–plastic fracture mechanics. For the loading and fatigue simulations the model parameters are obtained using a cyclic stress–strain curve taken from the literature. Only isotropic hardening behavior is assumed. Chawla et al. investigated the Bauschinger effect at a Fe–Mo–Cu–Ni alloy. Surface replication studies indicated that the observed Bauschinger behavior could be attributed to microscopic damage [9]. Chawla and Deng presented FEA-simulations based on a meshed microstructure. Hysteresis loops calculated for isotropic, linear kinematic and combined hardening for two densities are presented. The knowledge of the fully dense stress–strain behavior is used as the initial constitutive behavior [10,12]. According to the knowledge of the present authors, the cyclic plasticity is not verified for industrial PM materials. Due to microstructural stress concentrations induced by high porosity, PM-materials display a generally low ductility.

The present work aims to combine experimental data on a specially designed pure iron powder (ASC 100.29) with computational modeling to study the feasibility of the conventional cyclic plasticity model. The parameters of the material model are identified from experiments. Measured and calculated hysteresis loops are compared concerning different hardening mechanism. Cyclic stress–strain curves and corresponding fatigue life curves are presented. Effects of different densities and loading ratios are investigated.

## 2. Specimen fabrication

The specimens are produced from Hoeganaes ASC 100.29 powder (pure iron). The theoretical density is $\rho = 7.86$ g/cm$^3$. This powder is produced by water-atomization. During that process liquid iron is atomized together with water. The size-distribution of the particles follows a logarithmic normal distribution. The specimens are produced by die-pressing and sintering. Before die-pressing the powder is mixed with a lubricant (0.6% HDL-wax) to reduce the internal (particle–particle) and the external (particle-die) friction. This addition improves the density distribution and reduces the compaction pressure. The desired density can be controlled by the compaction pressure or the punch position. The density is determined with the Archimedes principle. Caused by the need of ejection, many die-compacted PM-parts have a simple 2D-shape. This leads to the rectangular cross-section of PM-specimen. Fig. 1 sketches the nominal specimen geometry used in the present work. The thickness, $b$, and the other dimensions of the specimen may vary since during the compaction (spring-back) and the sintering (shrinkage) a minor dimensional change takes place. The specimen average thickness is $b = 6$ mm. Two densities are realized, $\rho = 7.2$ g/cm$^3$ and $\rho = 6.8$ g/cm$^3$.

Fig. 2 shows the microstructures, in particular the material porosity. The 2D pore area corresponds to the void volume fraction (density). The metallic matrix is ferritic. The sintering takes place in a continuous conveyor belt furnace. By means of the belt velocity the sintering time can be affected. The ferritic matrix contains a multiplicity of pores. The density, the pore size and its shape are correlated. With decreasing pore size the pore shape factor increases while the pore size depends on the density. A major part of the porosity is open. That means that the pores form an open channel network [23].

An isothermal sintering temperature of $\theta = 1120$ °C and an isothermal sintering time of $t = 20$ min ($v = 10$ m/h) are chosen. Fig. 3 shows the employed sintering-profiles. The temperature is measured with long thermocouples (Ni–Cr–Ni). The sintering-profile (temperature/time) can be divided in three parts: dewaxing time, sintering time and cooling time. A slow increasing of temperature is characteristic for the dewaxing zone. In that zone the wax in the material is removed by evaporation. A high constant temperature is characteristic for the sintering zone. After the sintering the temperature decreases rapidly. During that process the hot parts are cooled down by a gas stream. Different microstructures can be realized by affecting the heat-transferring. The sintering
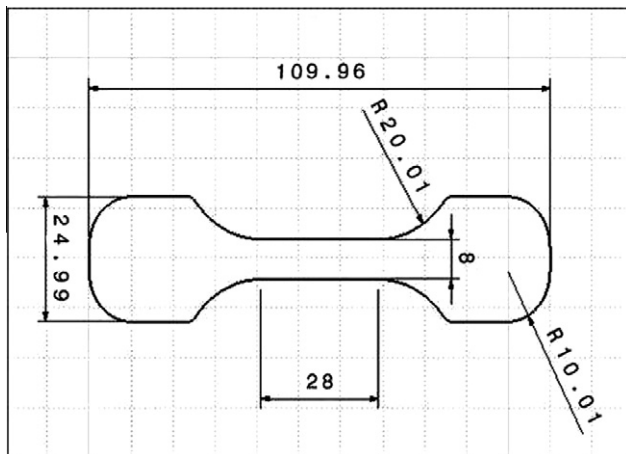


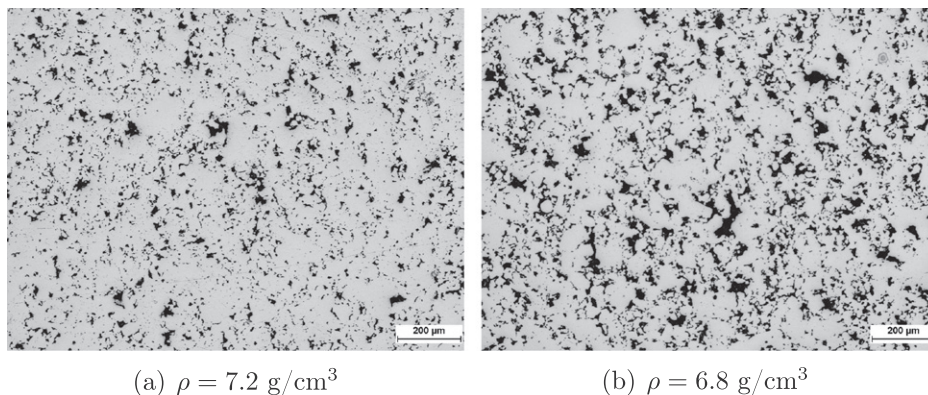**Fig. 1.** The nominal dimensions (in mm) of the specimen. The applied gage length is $L_0 = 25$ mm.



(a) $\rho = 7.2$ g/cm$^3$        (b) $\rho = 6.8$ g/cm$^3$

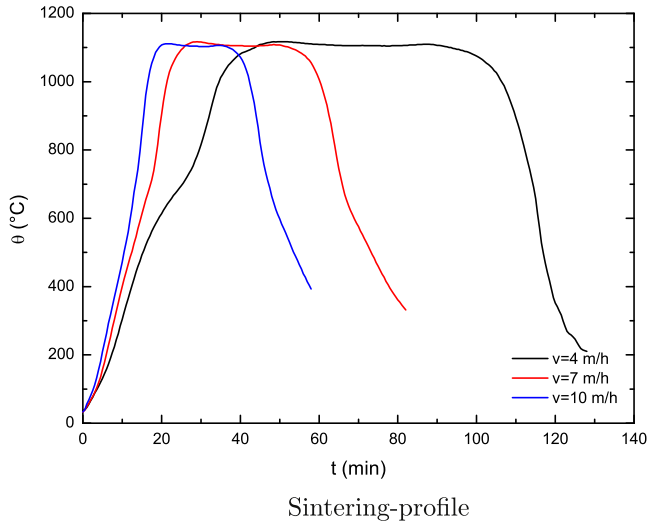**Fig. 2.** Microstructure of ASC 100.29.

Sintering-profile

**Fig. 3.** The influence of different belt velocities on the sintering time. A belt velocity of $v = 10$ m/h leads to an isothermal sintering time of $t = 20$ min. With an increasing belt velocity the dewaxing time becomes negligible.

**Table 1**
Carbon content of ASC 100.29 after the sintering.

| $\rho$ (g/cm$^3$) | $C_{surface}$ (%) | $C_{core}$ (%) |
|---|---|---|
| 7.2 | 0.0058 | 0.0001 |
| 6.8 | 0.0184 | 0.0088 |

atmosphere consists of 95% $N_2$ + 5% $H_2$ and 200 $l/h$ $CH_4$ concerning the dew point and its protective character. $CH_4$ is added because that furnace tends to decarburize PM-materials. The carburization effect on plain iron is given in Table 1. The carbon content is analyzed with a Leco CS-200 carbon determinator. The two density variants show a very low carburization effect. The carbon content close to the surface is higher than the carbon content in the core. Lower densities tend to absorb more carbon. Fig. 4 shows the Nital etched microstructures. These settings are typical for the PM-industry. Pure iron powder is not sensitive to different cooling rates, so it is suitable for general analysis.

## 3. Experiments

The strain-controlled cyclic tests were performed on a conventional mechanical testing machine of Zwick/Roell GmbH. The test frequency depends on the applied strain and the strain rate ($f \leqslant 0.1$ Hz). Two loading ratios are considered: $R_\epsilon = \epsilon_{min}/\epsilon_{max} = -1$
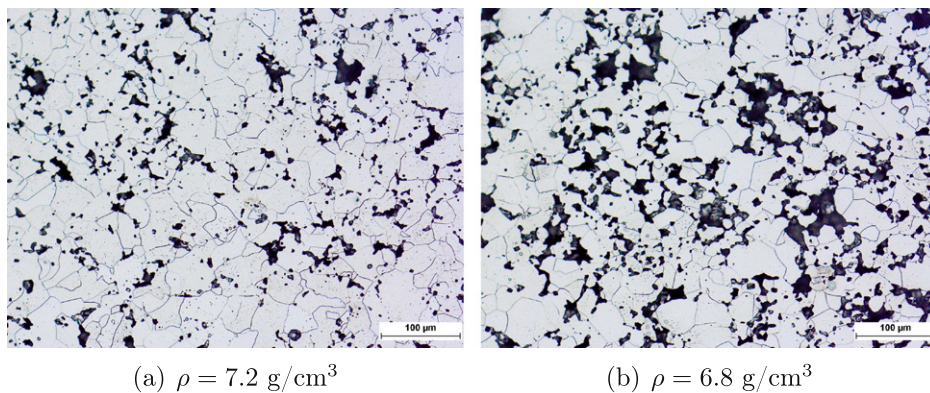
and 0, respectively. Additional experiments with notched specimen are performed under stress-controlled loading conditions with a stress loading ratio of $R_\sigma = \sigma_{min}/\sigma_{max} = 0$. An extensometer with $\Delta L_{max} = 30$ mm is used to measure and control the elongation. The gage length is in all cases $L_0 = 25$ mm. The force is measured and controlled by an $F_{max} = 200$ kN force transducer.

### 3.1. Cyclic stress–strain curves

Fig. 5 gives an exemplary overview of the hardening at two different loading ratios ($R_\epsilon = -1$ and 0, respectively) for a strain amplitude of $\epsilon_a = 0.5\%$. After the first cycle the phenomenon of relaxation of mean stress occurs. Subsequently the material is hardening. With increasing strain amplitude this effect becomes more insignificant. From the figures the effect of strain loading ratio can only be observed in the first cycles. After a few cycles the stress–strain relation becomes independent of loading ratio.

The sintered materials under cyclic loading condition show significantly different behavior from that under the monotonic loading. In Fig. 6 the monotonic and the cyclic stress–strain curves for two densities ($\rho = 6.8$ and 7.2 g/cm$^3$) are summarized under $R_\epsilon = -1$ and $R_\epsilon = 0$. The highest realized strain amplitude is $\epsilon_a = 1\%$ due to specimen buckling. The specimen is too small to apply higher compressive loading amplitudes. The experiments display that both materials are cyclically softened only for very low strain amplitudes $\epsilon_a \leqslant 0.5\%$, as reported in [18]. For higher loading the materials are significantly hardened. The cyclic values are fitted by the Ramberg–Osgood relation:

$$\epsilon_a = \frac{\sigma_a}{E} + \left(\frac{\sigma_a}{K'}\right)^{1/n'} \qquad (1)$$

where $\sigma_a$ is the uniaxial stress amplitude, $\epsilon_a$ is the uniaxial strain amplitude, $E$ is Young's modulus, $K'$ the strength coefficient and $n'$ is the strain hardening exponent. The fitted parameters are given in Table 2. In general, cyclic stress–strain curves are realized with a loading ratio of $R_\epsilon = -1$. Fig. 6 reveals that both curves with $R_\epsilon = -1$ and $R_\epsilon = 0$ are congruent. This means that there is no effect of the mean strain on the cyclic stress–strain relation.

### 3.2. The $\epsilon - N$ curves

The uniaxial fatigue tests ran at room temperature under strain-controlled conditions. Fig. 7 shows the corresponding fatigue strain life curves for both densities ($\rho = 6.8$ and 7.2 g/cm$^3$). The experimental data are fitted with the Manson-Coffin model:

$$\frac{\Delta\epsilon}{2} = \frac{\sigma_f'}{E}(2N_f)^b + \epsilon_f'(2N_f)^c, \qquad (2)$$



(a) $\rho = 7.2$ g/cm$^3$      (b) $\rho = 6.8$ g/cm$^3$

**Fig. 4.** Nital etched microstructure of ASC 100.29.

(a) $\rho = 7.2 \text{ g/cm}^3$, $R_\epsilon = -1$      (b) $\rho = 7.2 \text{ g/cm}^3$, $R_\epsilon = 0$
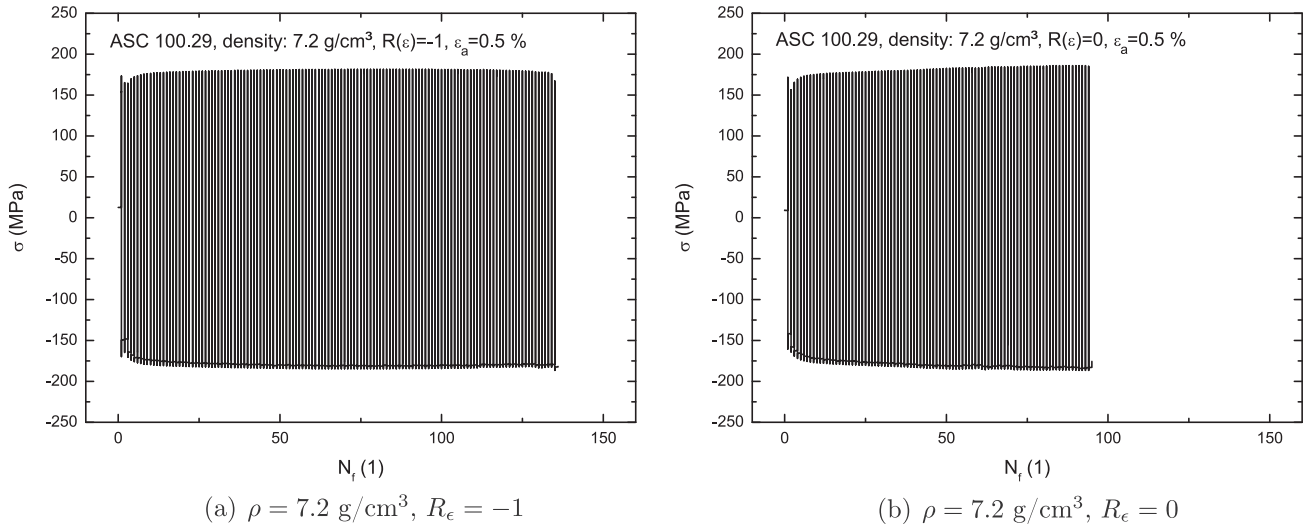
**Fig. 5.** Stress cycle curves of ASC 100.29. The effect of mean stress relaxation occurs only at the beginning. After a few cycles the stress response is symmetric for both loading ratios.
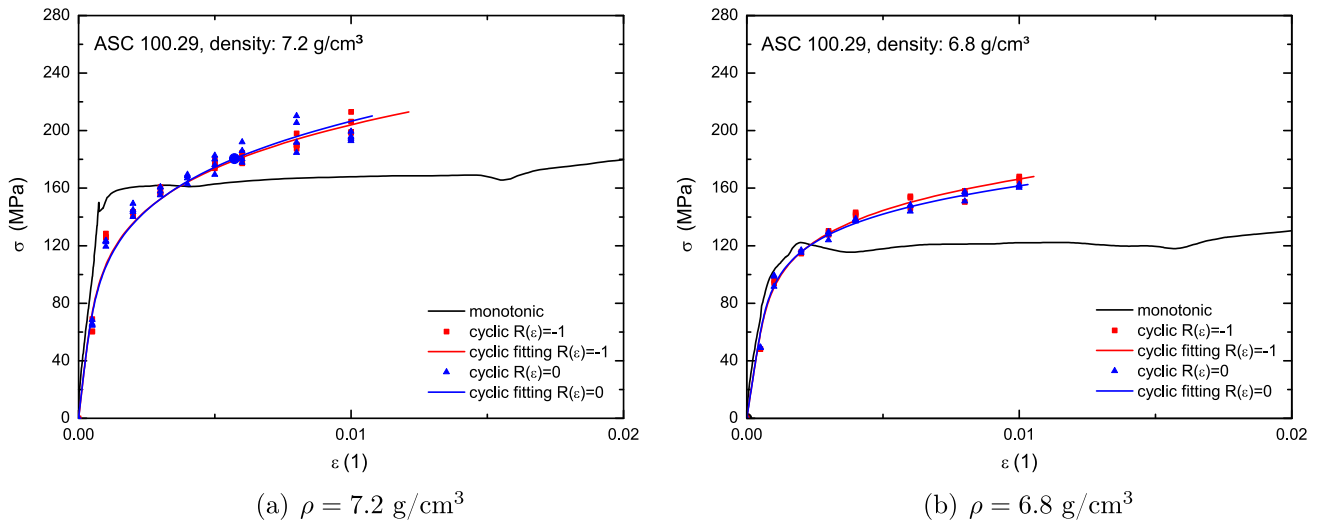


(a) $\rho = 7.2 \text{ g/cm}^3$      (b) $\rho = 6.8 \text{ g/cm}^3$

**Fig. 6.** Monotonic and cyclic stress–strain curves of ASC 100.29. Tests illustrate significant difference of the monotonic stress–strain curves from the cyclic curves. Both density variants show a cyclically hardening behavior above the yield point elongation. The curves are limited to $\epsilon$ = 2%, the fracture strains are $\epsilon_F$ = 10% for a density of 7.2 g/cm$^3$ and $\epsilon_F$ = 9% for a density of 6.8 g/cm$^3$. The mechanical properties, e.g. yield strength, tensile strength and fracture strain, depend on the density. These fitting curves offer an easy possibility to construct hysteresis loops with Masing's hypothesis.

**Table 2**
Ramberg–Osgood and Manson-Coffin parameters of ASC 100.29.

| $\rho$ (g/cm$^3$) | $R_\epsilon$ | $E$ (MPa) | $v$ | $K'$ (MPa) | $n'$ | $\epsilon'_f$ | $c$ |
|---|---|---|---|---|---|---|---|
| 7.2 | −1 | 165,000 | 0.272 | 533 | 0.20 | 0.029 | −0.35 |
| 7.2 | 0 | 165,000 | 0.272 | 562 | 0.21 | 0.024 | −0.32 |
| 6.8 | −1 | 123,000 | 0.260 | 379 | 0.17 | 0.028 | −0.39 |
| 6.8 | 0 | 123,000 | 0.260 | 344 | 0.16 | 0.027 | −0.38 |

where $\Delta\epsilon = 2\epsilon_a$ is the strain range, $N_f$ is the cycles to failure, $\sigma'_f$ is the fatigue strength coefficient, $b$ is the fatigue strength exponent, $\epsilon'_f$ is the fatigue ductility coefficient and $c$ is the fatigue ductility exponent. The equation requires four empirical constants. To reduce the number of free parameters it is common to relate them with the cyclic Ramberg–Osgood parameters as follows (equating coefficients) [21]:

$$K' = \frac{\sigma'_f}{\left(\epsilon'_f\right)^{n'}}, \quad n' = \frac{b}{c}. \tag{3}$$

It should be mentioned that the fatigue ductility exponent $c$ is higher than expected. A rough estimate predicts values between $c$ = −0.5 and $c$ = −0.7 [2]. Similar to the cyclic stress–strain curves the plotted fatigue strain life curves for $R_\epsilon$ = −1 and $R_\epsilon$ = 0 are congruent. All parameters for the Manson-Coffin model are independent of the mean stress.

## 4. Computations

The mechanical behavior of the present materials is assumed to be isotropic. A constitutive model based on higher-order strain is beyond the scope of the present paper. As the first step the conventional combined hardening model [1] is used to fit the cyclic plastic property of the materials. Young's modulus $E$ is measured by monotonic tensile tests. The slope is determined with a straight line which approximates the measured points with the least square method. Poisson's ratio $v$ is taken from a fitting curve which takes the strong dependency of the density into account [3].

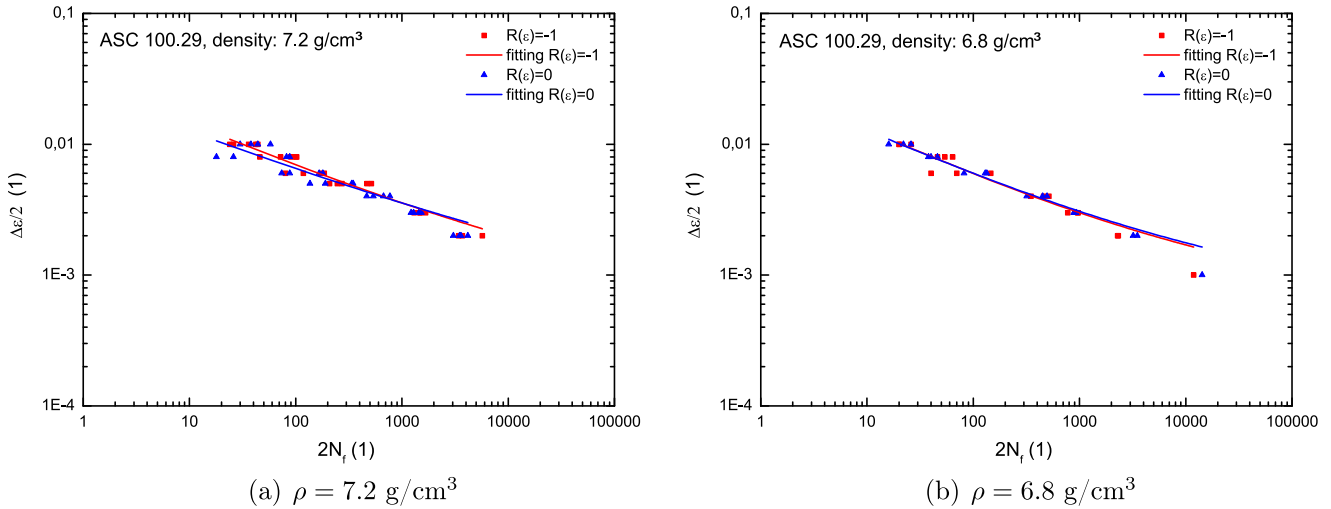(a) $\rho = 7.2$ g/cm$^3$      (b) $\rho = 6.8$ g/cm$^3$

**Fig. 7.** Fatigue strain life curves of ASC 100.29. Both curves with $R_\epsilon = -1$ and $R_\epsilon = 0$ are congruent. That means that there is no effect of mean strain to the fatigue life of the material. The reversals to failure for a given strain amplitude depend also on the density.

### 4.1. Identification of kinematic hardening parameters

To capture the Bauschinger effect the kinematic hardening has to be considered in the plasticity model [24]. The uniaxial stress amplitude for a stable hysteresis loop (combined hardening model) is given with:

$$\sigma_a = k_0 + Q + \alpha. \tag{4}$$

The material parameters can be determined based on both monotonic and cyclic stress–strain curves [26]. This model is especially of interest if the stress–strain loops are insufficiently available. A better fit will be estimated by taking different hysteresis loops into account. ABAQUS recommends a routine for every strain amplitude separately [1]. The advantage of this method is a good agreement for the chosen strain amplitude. The disadvantage is that these parameters are not valid for every other strain amplitude. This work deals with a more general routine. The parameter identification for the nonlinear kinematic hardening model is done with Lemaitre's equation of saturation behavior of the backstress $\alpha$ over the plastic strain range $\Delta\epsilon_p$. The saturation should follow a hyperbolic tangent:

$$\alpha = \frac{\Delta\sigma}{2} - k = \frac{C}{\gamma} \tanh\left(\frac{\gamma\Delta\epsilon_p}{2}\right). \tag{5}$$

There are three parameters to identify: the size of the elastic domain $2k$, asymptotic value of saturation $C/\gamma$ and a coefficient $\gamma$ which describes the slope [17]. The fitted values for pure iron are summarized in Table 3.

Characteristic material coefficients are identified by tension/compression tests from stabilized hysteresis loops, with respect to different strain amplitudes with the loading ratio $R_\epsilon = -1$. It is assumed that hysteresis loops stabilize after about $N = 100$ cycles.
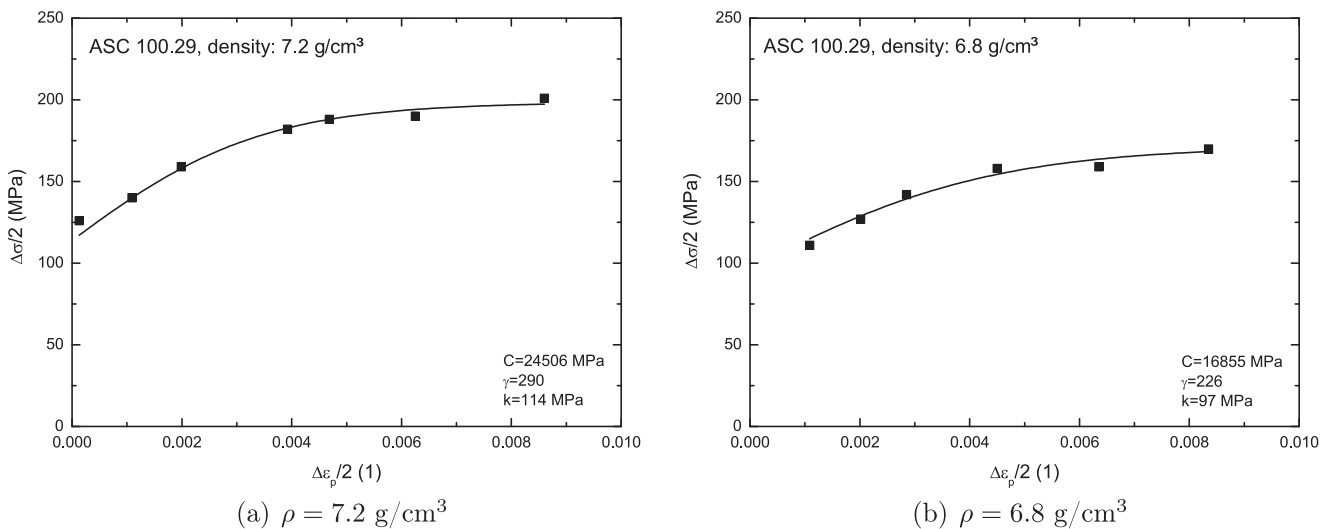
**Table 3**
Nonlinear kinematic hardening parameters of ASC 100.29.

| $\rho$ (g/cm$^3$) | $k$ (MPa) | $C$ (MPa) | $\gamma$ |
|---|---|---|---|
| 7.2 | 114 | 24,506 | 290 |
| 6.8 | 97 | 16,855 | 226 |



(a) $\rho = 7.2$ g/cm$^3$      (b) $\rho = 6.8$ g/cm$^3$

**Fig. 8.** Identification of nonlinear kinematic hardening parameters of ASC 100.29. The diagrams show the determination of the asymptotic value $C/\gamma + k$. With increasing density the value of $C/\gamma + k$ increases either. $\Delta\epsilon_p$ is taken from stabilized hysteresis loops. The plastic strain component can be found as the intersection points between the loop and the $\epsilon$-axis at a loading ratio of $R_\epsilon = -1$.

For $N_f/2 < 100$ the loops of $N_f/2$ are taken for the identification, as suggested in [15]. Note that all equations are calculated with engineering stresses and engineering strains. Due to small fracture strain, the difference to the true stress is negligible. The size of the elastic domain, $2k$, is measured on each cycle unloading in the realized strain-range. With respect to a small amount of
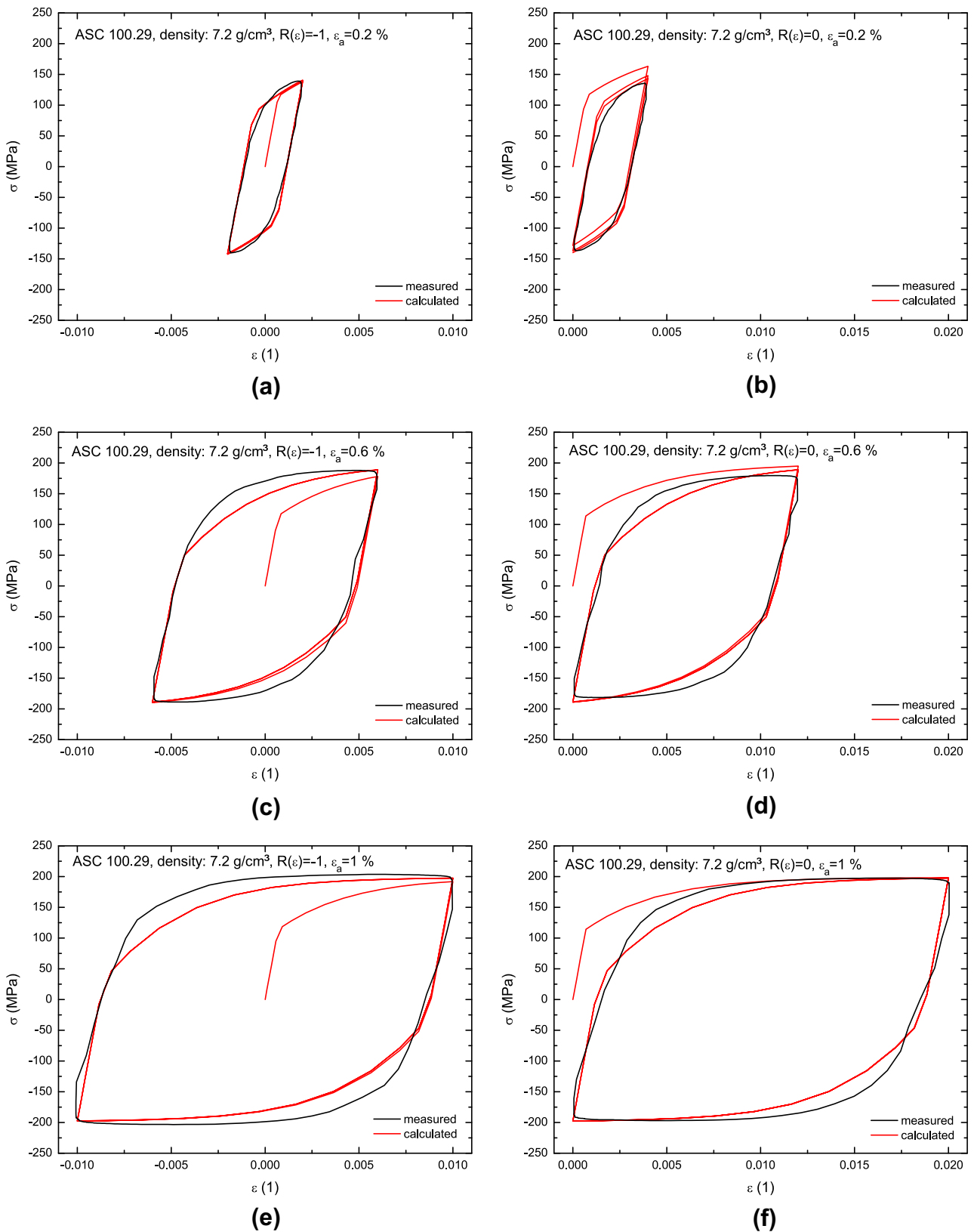


**Fig. 9.** Comparison of experiments at $N = 100$ to the computational results for three strain amplitudes $\epsilon_a = 0.2\%$, $\epsilon_a = 0.6\%$ and $\epsilon_a = 1\%$ of ASC 100.29 with a density of $\rho = 7.2$ g/cm³. Two loading ratios, $R_\epsilon = -1$ ((a), (c), (e)) and $R_\epsilon = 0$ ((b), (d), (f)), are investigated.

isotropic hardening the elastic domain is not constant. For taking this fact into account the elastic domain is calculated as an average over all measured elastic domains. Only at small strain-ranges when $2k \approx \Delta\sigma$, the corresponding data point is neglected because of an approximately pure elastic behavior. This yield strength is higher than the initial yield strength determined at the first hysteresis loop because of isotropic hardening [17]. Fig. 8 demonstrates the present evolution of $\Delta\sigma/2$. The evolution of the backstress $\alpha$ can be obtained by shifting the curve to the origin.

### 4.2. Prediction of stress–strain hysteresis loops

The combined hardening model of ABAQUS has been applied to predict the whole cyclic stress–strain curves, whereas the kinematic hardening should model stabilized stress–strain loops. Fig. 9 illustrates experimental records and computational results for the material with $\rho = 7.2$ g/cm$^3$. The material density will not affect the computational predictions. The computations are based on the model parameters given in Table 3. As stated, the material parameters are identified for the loading ratio of $R_\epsilon = -1$. The kinematic hardening model gives stabilized hysteresis loops after the first cycle, hence the calculated results are compared with cycle $N = 100$. Obviously, the computational model can predict the higher loading ratio with the same accuracy.

### 4.3. Identification of isotropic hardening parameters

With increasing applied loading, the material demonstrates substantial cold-work hardening behavior, which has to be considered in the isotropic hardening model. The cold-work effect can be described as an expansion of the elastic domain in the stress space [17]. To improve the elastic domain it is necessary to vary $k$ with the accumulated plastic strain $p$. If $\Delta\epsilon_p$ is the plastic strain-range over a cycle, the accumulated plastic strain for $N$ cycles is $p = 2N\Delta\epsilon_p \approx constant$. The initial elastic domain after the first cycle is $2k_0$. When the accumulated plastic strain becomes high, a stable value $k_0 + Q$ is reached. The parameter $b$ describes the rate of stabilization, as

$$k = k_0 + Q(1 - \exp(-bp)). \qquad (6)$$

Three different strain amplitudes (each with at least $N = 7$ cycles), $\epsilon_a = 0.6\%$, $\epsilon_a = 0.8\%$ and $\epsilon_a = 1\%$, are investigated. The fitting is performed at a loading ratio of $R_\epsilon = -1$.

The prediction of isotropic hardening is illustrated in Fig. 10, together with experimental data [8]. In the figures two different material densities ($\rho = 7.2$ and $6.8$ g/cm$^3$) and three strain amplitudes ($\epsilon_a = 0.6\%$, $0.8\%$ and $1\%$) are considered. In the calculation of the plastic strain, the variation of the elastic strain from cycle to cycle is neglected. The accumulated plastic strain is then equal to $p = 2N\Delta\epsilon_p$, which may introduce small deviations into the results. Both diagrams show rather convincing agreement between experiments and the simple hardening model, Eq. (6). The model parameters are independent of loading ratio, but affected by the mass density, as summarized in Table 4. For stress-controlled cyclic loading cases the isotropic behavior in the plasticity is of significance, as illustrated in the next section.

### 4.4. Prediction of cyclic elastic–plastic behavior

Summarizing both kinematic and isotropic hardening models, the combined hardening model should be able to predict whole cyclic tests. In Fig. 11a, c and e the first 10 loading cycles for strain-controlled cyclic tests are plotted for $R_\epsilon = 0$ and $\rho = 7.2$ g/cm$^3$. The computations plotted in Fig. 11b, d and f are conducted using the identified material parameters summarized in Tables 3 and 4. The superposition of the nonlinear kinematic model and the isotropic hardening model leads to a combined hardening behavior [17]. From the figures one observes two essential curve characteristics: translations and expansions of the yield surface. The whole transitions from the first loading cycle to stabilization in the computations differ from those of experiments.

Significant deviations can be observed even in the first loading cycle. The experimental stress for the first cycle is higher than that from the computations. The material is hardening much quicker than the computational model predicts for the small plastic strain. The plastic strain hardening in the experiments for the small plastic strain is significantly higher than the computational prediction

**Table 4**
Isotropic hardening parameters of ASC 100.29.

| $\rho$ (g/cm$^3$) | $k_0$ (MPa) | $Q$ (MPa) | $b$ |
|---|---|---|---|
| 7.2 | 89 | 50 | 17 |
| 6.8 | 76 | 50 | 14 |

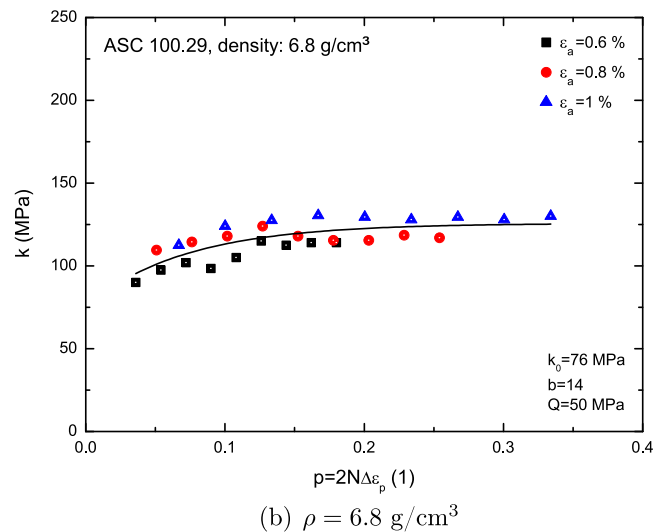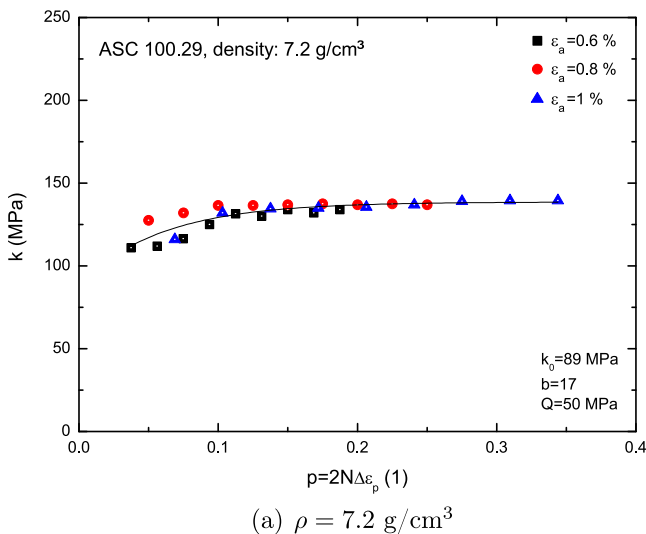

(a) $\rho = 7.2$ g/cm$^3$

(b) $\rho = 6.8$ g/cm$^3$

**Fig. 10.** Identification of isotropic hardening parameters. The diagrams show comparison of experiments (symbols) with a fitting of the isotropic hardening model, Eq. (6). It is assumed that $\Delta\epsilon_p$ is constant for the given strain amplitudes, $\epsilon_a = 0.6\%$, $0.8\%$ and $1\%$. For each strain amplitude up to $N = 10$ cycles are investigated.

(a) Experiment with $\epsilon_a = 0.2\%$

(b) Prediction for $\epsilon_a = 0.2\%$

(c) Experiment with $\epsilon_a = 0.6\%$

(d) Prediction for $\epsilon_a = 0.6\%$

(e) Experiment with $\epsilon_a = 1\%$

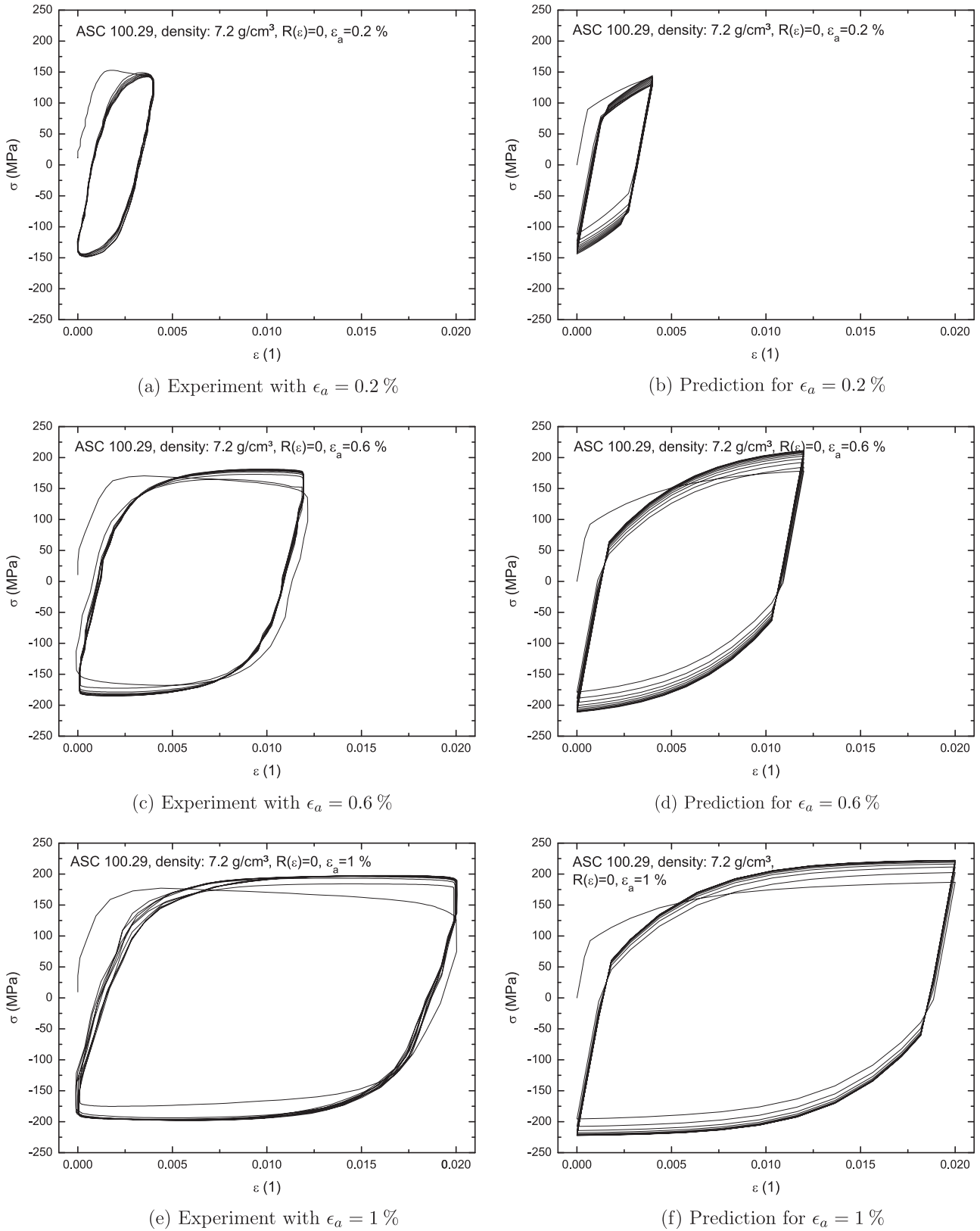(f) Prediction for $\epsilon_a = 1\%$

**Fig. 11.** The first 10 loading cycles measured in tests ((a), (c), (e)) and predicted based on the combined hardening model ((b), (d), (f)) for three strain amplitudes, $\epsilon_a = 0.2\%$, 0.6% and 1%, with a density of $\rho = 7.2$ g/cm³. The loading ratio is $R_\epsilon = 0$.

which cannot be changed due to fixing the strain hardening exponent in cyclic loading. Furthermore, the experiments show softening in the first loading cycle with further increasing plastification, whereas the computations reveal a uniform hardening pattern.

This hardening effect relaxes after one cycle and then the hysteresis loop assumes a stable shape. More results for different mass density is reported in Fig. 12 which shows the same observation. This phenomenon could be related to Lüders band building.
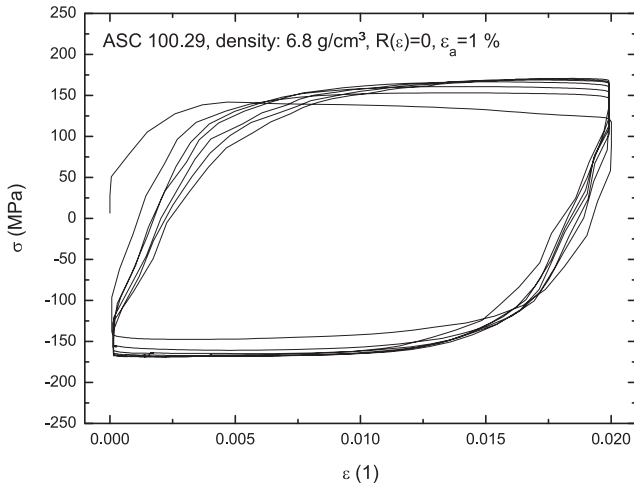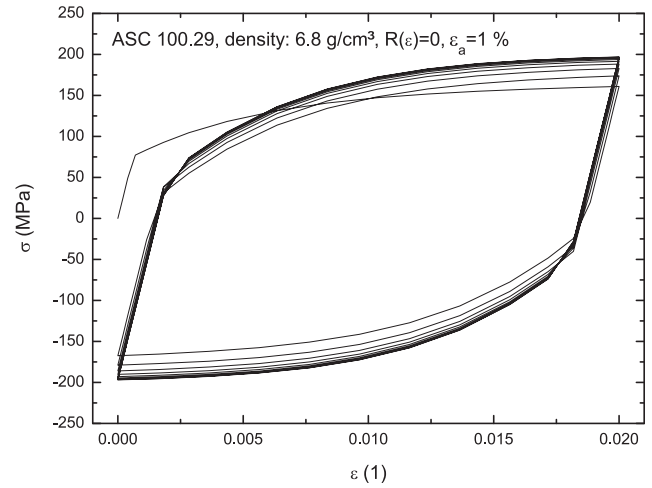
(a) Experiment with $\epsilon_a = 1\%$    (b) Prediction for $\epsilon_a = 1\%$

**Fig. 12.** The first 10 loading cycles measured in tests (a) and predicted based on the combined hardening model (b) for one strain amplitude, $\epsilon_a = 1\%$, with a density of $\rho = 6.8$ g/cm³. The loading ratio is $R_\epsilon = 0$.
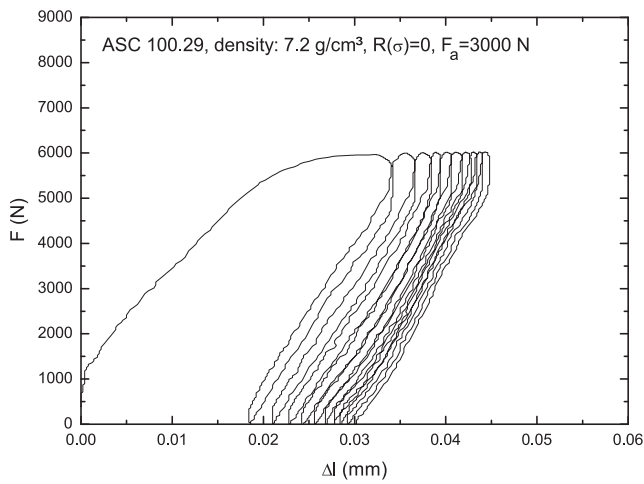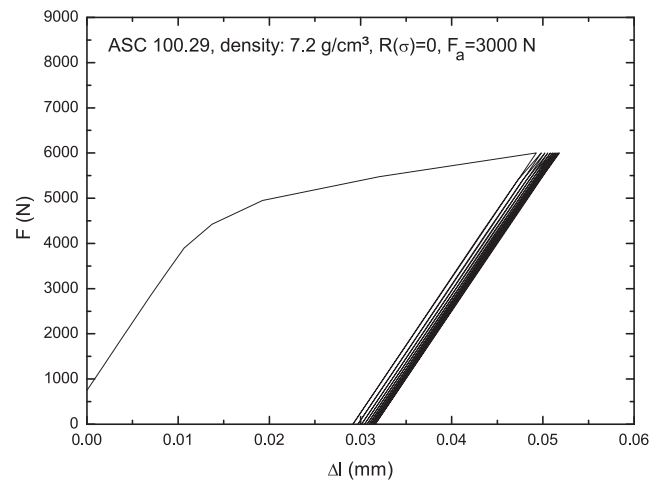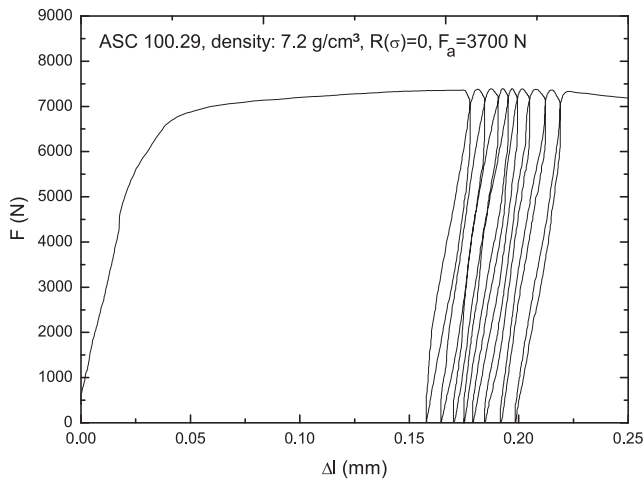


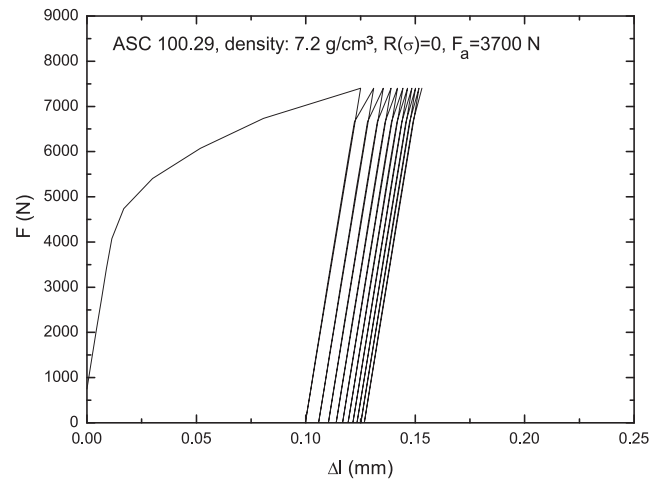(a) Experiment with $\sigma_a = 84.8$ MPa    (b) Prediction for $\sigma_a = 84.8$ MPa

(c) Experiment with $\sigma_a = 104.5$ MPa    (d) Prediction for $\sigma_a = 104.5$ MPa

**Fig. 13.** Comparison of experimental and computational results of the notched tensile specimen; (a) and (c) show experimental results, (b) and (d) show computational prediction based on the combined hardening model. $\rho = 7.2$ g/cm³ and $R_\sigma = 0$.

With number of cycles the plastic strain hardening exponent grows, as shown in Fig. 11a, c and e. Generally the PM materials show varying plastic strain hardening exponents. Using the present simple cyclic plasticity model the approximation is still satisfactory. However, the model cannot adopt a perfect plastic behavior, so the model predicts direct hardening. This is the reason for the different hardening modulus. The calculated maximun/minimum stress values are overestimated. The reasons are the superposition of two hardening models and the higher hardening modulus as mentioned above.

### 4.5. Verification with notched specimens

The identified plasticity model is to be verified in experiments with notched specimens performed under stress-controlled loading conditions. The specimen illustrated in Fig. 1 is modified by drilling a circular hole with a diameter of $d = 2.1$ mm in the center of the specimen. Caused by the mechanical testing machine a non-zero axial force occurs during the gripping. The offset-force depends on the material density, $F_{offset}$ ($\rho = 7.2$ g/cm$^3$) $\approx 750$ N. This will induce small deviations in comparison of results. The theoretical stress concentration factor is $K_t \approx 2.4$ [20]. Stress controlled tests with different force amplitudes $\sigma_a = F_a/A_0$ with a loading ratio of $R_\sigma = 0$ are realized. $A_0$ denotes the initial cross section area of the specimen. The material response is expressed in terms of reaction force $F$ and displacement $\Delta l$. Experimental records and computational predictions are collected in Fig. 13 for the material ASC 100.29 with a density of $\rho = 7.2$ g/cm$^3$.

The nominal stress–strain curves of the experiments reveal that the specimen is not hardened from plastification so significantly as in the computations. Due to the high hardening response of the materials for the small strain region, as observed in the uniaxial tension (Figs. 11 and 12), the computations predict obviously larger deformations at a given applied load, as shown in Fig. 13. With increasing plastifications, the material gets less hardened and even weakly softened (Fig. 6), with results in less growth of the force–displacement curves in high loading cases. The situation at higher loading becomes different, that is, the computational predicted strain at $\sigma_a = 104.5$ MPa is smaller than the experimental data since the material demonstrates softening in the monotonic loading process.

Additionally the experiments reveal ratcheting effects from the first loading on. Whereas the lower loading diagram intends stabilization, the higher loading leads to total failure after eight loading cycles. In the latter the ratcheting phenomenon may be related to the cyclic microcrack propagation. The micro-mechanism remains to be clarified. The computational prediction from the combined hardening model is unsatisfactory in this case. The predicted ratcheting effects are much too small and tend to be stabilized too quick.

## 5. Conclusions

In the present work a powder metal ASC 100.29 has been investigated both experimentally and computationally. Two different material densities have been considered. Experiments are performed under uniaxial tension/compression conditions, whereas the computations are run using the conventional combined hardening model of ABAQUS. Based on the experimental and computational results the following conclusions can be drawn:

- The material demonstrates significant hardening both in the first cycle within very small strains and under cyclic loading conditions. The total hardening behavior cannot be described by a uniform hardening power-law. The material is strongly

cyclic hardened generally, whereas the first loading cycle shows softening for all tested conditions. The softening is observed, however, only in the first cycles with large deformation, i.e. beyond 0.05% nominal strains in the first loading cycle. Since the cyclic fracture strain of the material is small, effects of the Lüders band formation could play an important role in the initial hardening of the material. This feature makes a uniform plasticity model difficult.

- The stress–strain loops are stabilized rapidly. The stabilized loops can be described by the nonlinear kinematic hardening model and the isotropic hardening in a power-law form, as confirmed in the present work. The cyclic material behavior can be approximated by the combined hardening model reasonably. The accumulated plastic strain is a reasonable internal variable for the cyclic plasticity of the PM material.
- The cyclic elastic–plastic behavior as well as the fatigue life of the investigated PM materials are independent of the mean stress of the applied load. The Manson-Coffin model gives a good prediction of the obtained life model for the strain-controlled tests.
- Tests on notched specimens under stress-controlled loading condition show significant ratcheting effects. The cyclic material softening could be related to cyclic microcrack propagation due to microstress concentration in the highly porous material. Further detailed experiments are required to clarify the mechanism.
- Verification of the identified combined hardening model in the drilled tensile bar shows obvious deviations between experiments and computations. Due to the difference in the monotonic stress–strain curve, the predicted stress–strain loops display different developments of the curves.

## References

[1] ABAQUS User's Manual, Version 6.9., Simulia Inc., Providence, RI, 2009.
[2] J.A. Bannantine, Fundamentals of Metal Fatigue Analysis, first ed., Prentice Hall Englewood Cliffs, New Jersey, 1989.
[3] P. Beiss, Pulvermetallurgie: Material-Prozess-Anwendung, Pulvermetallurgie in Wissenschaft und Praxis, Band 19, S. 3-24, Fachverband Pulvermetallurgie, 2003.
[4] P. Beiss, M. Dalgic, Effect of pore structure on bending fatigue strength of sintered steel, Advances in Powder Metallurgy and Particulate Materials, vol. 4, MPIF/APMI, Princeton, NJ, 1996. pp. 13/249–13/257.
[5] P. Beiss, S. Lindlohr, Porosity statistics of extremes and fatigue strength of sintered iron, in: Advances in Powder Metallurgy and Particulate Materials, Proc. CD, Part 10, MPIF/APMI, Princeton, NJ, 2008, pp. 140–153.
[6] G.F. Bocchini, International Journal of Powder Metallurgy 22 (3) (1986) 185–202.
[7] U. Brandt, C.M. Sonsino, U. Engström, E. Ernst, E. Hoffmann, Development of high-strength P/M steels with optimized micro-structures by new alloying and sintering techniques, Advances in Powder Metallurgy and Particulate Materials, vol. 4, MPIF/APMI, Princeton, NJ, 1996. pp. 13/17–13/26.
[8] W. Brocks, Parameteridentifikation in der Werkstoffmechanik, 42. Tagung DVM-Arbeitskreis Bruchvorgänge, DVM-Bericht 242, DVM-Berlin, 2010, pp. 257–266.
[9] N. Chawla, B. Jester, D.T. Vonk, Materials Science and Engineering A346 (2003).
[10] N. Chawla, X. Deng, Materials Science and Engineering A390 (2005).
[11] H. Danninger, G. Jangg, B. Weiss, R. Stickler, Powder Metallurgy International 25 (4) (1993) 170–173.
[12] X. Deng, G.B. Piotrowski, J.J. Williams, N. Chawla, International Journal of Fatigue 27 (2005).
[13] G.E. Dieter, Mechanical Metallurgy, third ed., McGraw-Hill Companies, Inc., Boston, 2006.
[14] A. Hadrboletz, B. Weiss, International Materials Reviews 42 (1) (1997) 1–44.
[15] E. Haibach, Betriebsfestigkeit, Auflage, 3, Springer Verlag, Berlin/Heidelberg/ New York, 2006.
[16] T. Kraft, H. Riedel, Assessment of fatigue lifetime of PM-Parts, Proceedings of the 2004 World Congress on Powder Metallurgy, vol. 3, EPMA, Shrewsbury, UK, 2004. pp. 111–116.
[17] J. Lemaitre, J.-L. Chaboche, Mechanics of Solid Materials, first English ed., Cambridge University Press, Cambridge, 1990.
[18] D.A. Lados, D. Apelian, Key issues affecting the performance of P/M components during dynamic loading, in: Proceedings of the 2003 International Conference on Automotive Fatigue Design and Applications, MPIF/APMI, Princeton, NJ, 2003, pp. 49–67.

[19] P.M. Machmeier, T. Matuszewski, D.W. Smith, P.B. Lemens, H.R. Jhansale, Effect of P/M composition, processing and heat treatment parameters on pore-free P/F-46XX alloy steel fatigue behavior, Advances in Powder Metallurgy and Particulate Materials, vol. 4, MPIF/APMI, Princeton, NJ, 1993.

[20] R.E. Peterson, Stress Concentration Factors, first ed., John Wiley and Sons Inc., Hoboken, New Jersey, 1974.

[21] D. Radaj, Ermüdungsfestigkeit, Auflage, 1, Springer Verlag, Berlin/Heidelberg/New York, 1995.

[22] H. Rutz, T. Murphy, T. Cimino, The effect of microstructure on fatigue properties of high density ferrous P/M materials, Advances in Powder Metallurgy and Particulate Materials, vol. 4, MPIF/APMI, Princeton, NJ, 1996. pp. 13/375–13/389.

[23] M. Schneider, H. Yuan, Experimental and computational analysis of damage evoltion in porous sintered irons of miniature specimens, 42. Tagung DVM-Arbeitskreis Bruchvorgänge, DVM-Bericht 242, DVM-Berlin, 2010, pp. 61–72.

[24] J.C. Simo, Computational Inelasticity, second ed., Springer Verlag, Berlin/Heidelberg/New York, 2000.

[25] B. Weiss, H. Danninger, A. Hadrboletz, Review on the fatigue behaviour of pressed and sintered ferrous materials, in: Proceedings of the 1998 World Congress on Powder Metallurgy, 1998, pp. 135–141.

[26] H. Yuan, Computational Plasticity, first ed., Lecture Notes University of Wuppertal, Wuppertal, 2008.